

Anomalies in the Flow over Projectile with Wrap-around Fins

Ravi Krishna*, Rhishabh Surit**, Abhijit Kushari***, and A. K. Ghosh***

*Aerial Delivery Research and Development Establishment, Agra-282 001

**Ingrated Test Range, Chandipur-756 025

***Indian Institute of Technology, Kanpur-208 016

ABSTRACT

This paper presents the results of a numerical study to understand the flow field over a projectile with wrap-around fins. This investigation is performed in order to determine aerodynamic coefficients for the missile model for varying Mach number from 1.2 to 2.5. The roll moment coefficients were computed from the flow field solution and compared with other computational models and experimental works. The results show a reversal of the rolling moment in a Mach number from 1.2 to 1.4. While generating Mach number profile along missile body, a transition from subsonic to supersonic flow was notably found just before the fin-tip in the Mach number range from 1.2 to 1.4. This transition from subsonic to supersonic just before the fin seems to be the main cause for the roll reversal, which makes the flow inside the fin passage behave differently. Furthermore, it was seen that most of the effect was confined towards the leading edge of the fins.

Keywords: Wrap-around fins, roll reversal, shock structure, curved shock, projectile, missile model

NOMENCLATURE

A	Flux jacobian $\partial F / \partial Q$
CFL	Courant-Friedrichs-Lewy condition
D	Centre matrix
dA	Differential surface area
E	Total internal energy per unit mass
F	Inviscid flux vector
G	Shear stress vector
H	A vector containing source terms such as body forces and energy sources
H	Enthalpy
M	Modal matrix that diagonalizes $\Gamma^{-1}A$
N_{faces}	of faces (except boundary faces) in a grid
n	Time index
p	Pressure of fluid
Q	Primitive variables $\{p, u, v, w, T\}^T$
q	Heat flux
R^n	Residual vector
$S_{j,k}$	Off-diagonal coefficient matrix
u, v, w	Cartesian velocity components
V	Arbitrary control volume
v	Fluid velocity
W	State vector (flow variable vector)
ϵ	Error
Δt	Time step
Δx	Grid length
ρ	Density
τ	Stress tensor
Λ	Diagonal matrix of eigen values
Γ	Preconditioning matrix

λ_{max}	Maximum of the local eigen values
Σ	Laplacean smoothing operator

1. INTRODUCTION

With the development of different missiles, from ground-launched saturation field-artillery rockets to air-launched weapons, simple unguided rockets or sophisticated cruise missiles, tube launching was chosen for its packaging convenience and for increasing the reliability of the rocket motor. These projectiles require folding aerodynamic stabilisers because of packaging constraints. Such stabilisers would be folded in the stowed position to fit within a circular cylinder and would deploy instantly after launch. The wrap-around fin (WAF) configurations not only meet these requirements, they also maximise the volume available for the missile's subsystems, especially for the nozzle exit. Modern advances in stealth technology have made use of the missiles equipped with WAF desirable, because these can be stowed to reduce the radar cross-section of the aircraft [1]. These WAF configurations have conventional longitudinal aerodynamics similar to those with planar fins of identical planform [2]. However, several aerodynamic anomalies have been repeatedly experienced[3] during previous studies. Major ones include rolling moment at 0° angle of attack (AOA) [4,5], roll reversal at transonic conditions (around Mach No. 1.0-1.5)[5,6] and varying pitch-yaw-side force coupling experienced at varying AOA [7]. These anomalies have been one of the major causes of deviation of projectile from its prescribed trajectory. The spinning projectile experience torque due to the side

force, which is perpendicular to both torque applied and the angular momentum of the projectile, causing wobbling motion from its target [8]. Thus, to design dynamically stable projectiles, one need to predict these anomalies for all the flight conditions for flight trajectory.

Previous CFD studies [9-13] of missile configurations with WAF have shown general agreement with experimental data of roll reversal, but always lacked accuracy in roll moment and side moment determination. Edge [11] considered both inviscid as well as viscous flows and calculated the roll moment using a three-dimensional full Navier-Stokes code. Abate and Cook [12] calculated the roll moment of WAFs attached to an infinitely long cylinder using Euler code. They pointed out that the accuracy of CFD greatly depends on the configuration modelled. They also added that roll moment did not appear as long as fin thickness was neglected. So they considered fin thickness to be the critical parameter in WAF aerodynamics. They explained the roll moment reversal with the concept of converging diverging nozzle [12]. Paek[13], *et al.* further showed that the edge and tip shapes too have a great significance in the roll moment of WAF. They also showed that Euler equations can give comparably accurate solutions when computing the roll moment of WAF configuration. Their comparison with Edge [11] showed that the fin tip, when pinched, shows complete agreement with the experimental data.

Dahlke[14] conducted an experimental study on WAF for range of Mach number 0.3 to 3.0 and proved that the static longitudinal aerodynamic characteristics of WAF did not differ from conventional configuration with identical bodies and flat fins whose area was equal to the projected area of the curved fins. McIntyre [1], *et al* used experimental analogy to investigate the rolling moment reduction with increasing Mach number. They used Schlieren photography and surface flow visualisation of the fin-generated shock structure. For rolling moment reduction, they used two

curved fin missiles, one having a solid fin and the other a slotted fin. The slot was to provide pressure relief thereby reducing the Mach dependence of the rolling moment, and thus reduce the strength of shock structure produced by the fin. Results indicated that the magnitude of the rolling moment decreases with increasing Mach number for both the fins and rolling moment for the slotted fin reduced drastically along with a reduction in wave drag. Rolling moment is positive at subsonic velocity (missile roll towards the concave side of the fin) and roll reversal was experienced at about Mach No 1.0. Winchenbach [15], *et al.* conducted the free flight aeroballistics tests to obtain aerodynamic data over Mach number from 0.6 to 1.35 for a WAF configuration at atmospheric pressure. Results of their analysis indicated that dynamic instability exists above Mach No. 1 and is related to an out of plane side moment which is dependent on the pitch angle and this moment can have a dramatic effect on trajectory computations based on the conventional aerodynamic coefficient and derivatives. They observed detached bow shock formation at the fin tip and reasoned it to be the possible cause for rolling moment variation in view of varying flow field along concave and convex sides of the fin.

In spite of various works, the primary reason for roll reversal has not been properly explained. However, the computational simulation [16] and experimental studies [17] on a single WAF by Tilmann [16,17], *et al* suggest the vortex formation at the fin/body juncture at the convex side of the fin can be the cause of roll reversal. Abate and Cook [12] explained roll reversal phenomenon as converging-diverging analogy. However, if it would have been the reason, then roll reversal would have been reported at Mach No. 1.0 in ideal conditions. Furthermore, the roll reversal Mach number, reported by various researchers had never been consistent. Few previous computational works were been done while neglecting some important

Table 1. Computational and experimental work and a brief discussion on their respective models.

Data source	Model used	Roll reversal reported at Mach No.	Range of Mach on which experiment was done
JPL	TTCP configuration, with no boundary layer trips on fin-leading edge, free-flight data	1.8	0.6 - 3
AEDC	TTCP configuration, with boundary layer trips on fin-leading edge	1.1	0.5 - 1.4
NASA Langley	TTCP configuration, with boundary layer trips on fin-leading edge	Not Known	1.5 - 3
McDonnell Douglas	TTCP configuration, with boundary layer trips on fin-leading edge	Not Known	1.5 - 2.8
Abate & Cook	WAF modeled on infinitely long body, with 10% thick bi-convex fin	1	0.4 - 3.5
Paek, <i>et al.</i>	TTCP configuration, inviscid	1.7	1.2 - 2.5
Edge	TTCP configuration, viscous	1.7	1.25 - 2.5

parameters like viscous effects. The importance of proper configuration of mesh had been sometimes overlooked. The accuracy of CFD results greatly depends on how accurately the configuration was modelled, which has been taken care of in the present study.

A comparison of the available data on roll reversal is presented in Table 1. It should be pointed out that the JPL (Jet Propulsion Laboratory) is a free-flight data, whereas Arnold Engineering Development Centre (AEDC), NASA Langley Centre, and McDonnell Douglas are wind tunnel data. Abate and Cook[12], Paek[13], *et al* and Edge[11] are computational work. As shown in Table 1, no particular cross-over point has been uniformly observed. This can be attributed to how the configuration is modelled. In the present work, standard The Technical Co-operation Program (TTCP) model has been used, while considering viscous effects too. The focus of the present study is to understand the reason behind aerodynamic anomalies of WAF projectile. Computational mesh geometry was generated using GAMBIT, while processing and post-processing work was done using FLUENT®. Simulation work was carried from Mach number ranging from 0.8 to 2.5 to determine aerodynamics coefficients for missile model.

2. NUMERICAL FORMULATION

The system of governing equations for a single-component fluid, written to describe the mean flow properties, is cast in integral, Cartesian form for an arbitrary control volume V with differential surface area dA as follows:

$$\frac{\partial}{\partial t} \int_V W(Q) dV + \oint [F(Q) - G(Q)] dA = \int_V H dV \quad (1)$$

Where the W is the dependent vector of conserved variable, F and G are the inviscid and viscous flux vector in standard conservation form and Q is the dependent vectors of primary variables:

$$W = \begin{Bmatrix} \rho \\ \rho u \\ \rho v \\ \rho w \\ \rho E \end{Bmatrix}, F = \begin{Bmatrix} \rho v \\ \rho v u + p \hat{i} \\ \rho v v + p \hat{j} \\ \rho v \omega + p \hat{k} \\ \rho v E + p v \end{Bmatrix}, G = \begin{Bmatrix} 0 \\ \tau_{xi} \\ \tau_{yi} \\ \tau_{zi} \\ \tau_{ij} v_j + q \end{Bmatrix}, Q = \begin{Bmatrix} p \\ u \\ v \\ w \\ T \end{Bmatrix} \quad (2)$$

H is the total enthalpy per unit mass and is related to the total energy E by:

$$H = E + \frac{p}{\rho} \quad (3)$$

Equation (1) is numerically stiff and has slow rate of convergence in low Mach number region and incompressible flow region. This problem is alleviated by pre-multiplying the time-derivative term by a pre-conditioning matrix[18] Γ . The resulting governing equation becomes:

$$\Gamma \frac{\partial}{\partial t} \int_V Q dV + \oint [F(Q) - G(Q)] dA = \int_V H dV \quad (4)$$

$$\text{where } \Gamma = \frac{\partial W}{\partial Q} = \begin{bmatrix} \rho_p & 0 & 0 & 0 & \rho_T \\ \rho_p u & \rho & 0 & 0 & \rho_T u \\ \rho_p v & 0 & \rho & 0 & \rho_T v \\ \rho_p w & 0 & 0 & \rho & \rho_T w \\ \rho_p H - \delta & \rho u & \rho v & \rho w & \rho_T H + \rho C_p \end{bmatrix}$$

$$\rho_p = \left. \frac{\partial \rho}{\partial p} \right|_T, \rho_T = \left. \frac{\partial \rho}{\partial T} \right|_p$$

$\delta = 1$ for ideal gas and $\delta = 0$ for incompressible fluid.

The governing Eqn (5) is discretised spatially using a finite volume scheme wherein the physical domain is subdivided into cells and the integral equations are applied to each cell. The flow field is represented by associating with each cell an average value of the solution Q^i within the control volume. The flux vectors F and G appearing in Eqn (5) are evaluated by standard upwind, flux-difference splitting [19]. The discrete flux at each face of the control volume is obtained as:

$$F = \frac{1}{2} (F(Q_R) + F(Q_L)) - \frac{1}{2} \Gamma |\hat{A}| (Q_R - Q_L) \quad (5)$$

Where, Q_R and Q_L are the solution vector right and left side of the face,

$|\hat{A}| = M |\Lambda| M^{-1}$ (Λ is the diagonal matrix of eigen values and M is the modal matrix that diagonalises $\Gamma^{-1}A$, where A is the flux jacobian $\frac{\partial F}{\partial Q}$).

An Euler implicit discretisation in time (using first order upwinding scheme) of the governing equations is combined with a Newton-type linearisation of the fluxes to produce the following linearised system in delta form:

$$\left[D + \sum_j^{N_{\text{faces}}} S_{j,k} \right] \Delta Q^{n+1} = -R^n \quad (6)$$

The centre and off-diagonal coefficient matrices, D and $S_{j,k}$ are given by,

$$D = \frac{V}{\Delta t} \Gamma + \sum_j^{N_{\text{faces}}} S_{j,i} \quad (7)$$

$$S_{j,k} = \left(\frac{\partial F_j}{\partial Q_k} - \frac{\partial G_j}{\partial Q_k} \right) \quad (8)$$

and the residual vector R^n and time step Δt are defined as,

$$R^n = \sum_j^{N_{\text{faces}}} (F(Q^n) - G(Q^n)) \cdot A \cdot V H \quad (9)$$

$$\Delta t = \frac{CFL \Delta x}{\lambda_{\text{max}}} \quad (10)$$

It should be noted that the detailed derivation of the scheme is provided by Weiss, *et al* [20].

The above equations are solved using a point Gauss-Seidel scheme in conjunction with an algebraic multigrid (AMG) method [21] adapted for coupled sets of equations.

The fin projectile designed by TTCP was used as the basic configuration in the present study as shown in Fig. 1, which has a length of 200 cm and a diameter of 20 cm. It should be noted that the dimensions mentioned in Fig.1 are in calibers, and 1 caliber corresponds to 20 cm. The standard TTCP configuration has fins with symmetric leading and trailing edge bevels, with a difference of 45° exists between the root and tip chord cross section.

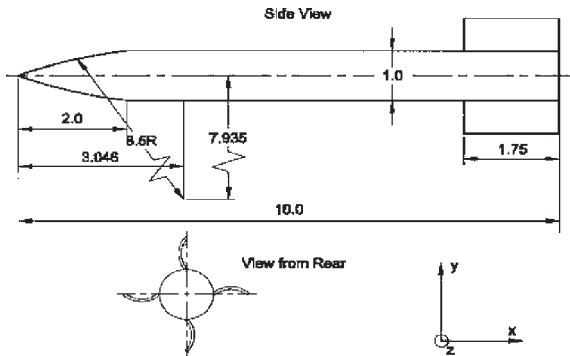


Figure 1. Geometry of TTCP standard model.

Previous computational studies [11,13] were done with blunt leading and trailing edges. In the present study, two configurations have been developed, one with blunt leading edge and the other with a pinched leading edge. Figures 2(a) and 2(b) show the fin shape for both pinched and blunt model respectively.

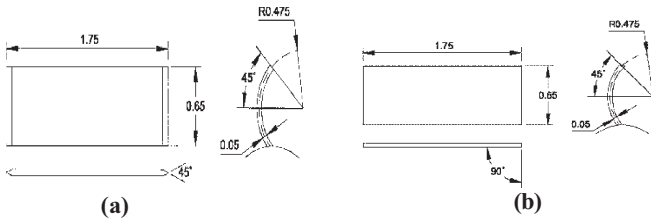


Figure 2. Fin shape of TTCP standard model: (a) pinched model and (b) blunt model.

The complete projectile model computational grid was generated using GAMBIT®. Since the mesh geometry needed to be focused towards the fin-tip, fin-thickness, and fin-area, dense meshing was done in the near-region of projectile model. Computational domain surrounding the model was chosen in the shape of a cylinder of 5 units. Another cylinder was created of 2 units enclosing the model. This cylinder was meshed with finer grid size, whereas outer cylinder was coarsely meshed. This enabled in getting a clustered grid in the fin-vicinity, thus, providing accurate results. For meshing the surface of the missile, quadrilateral meshing with map and pave scheme was used, in addition with a spacing function relating with the surface. For the flow field meshing, structured meshing scheme employing Hexahedral map and Hexahedral cooper



Figure 3. Meshing of body surface of standard TTCP projectile.

was used. Figure 3 shows meshing on the body surface of a standard TTCP projectile.

Figures 4(a) to (c) show detailed view of the mesh over the nose and fin surface of the missile (both blunt and pinched) and Fig. 5 shows the flow field mesh in the vicinity of the fin.

Different boundary conditions were defined for different faces. The model surfaces were defined as walls, while the inlet and the outlet faces were defined as pressure inlet and pressure outlet conditions respectively as required by the compressible flow formulation being used in the present study. Processing and post-processing were done using FLUENT®. Steady-state solution was achieved using coupled implicit formulation involving the energy Eqn (1) which is the requirement of compressible high speed flow as it captures the shock pattern efficiently. The velocity formulation was chosen to be absolute and Green-Gauss cell-based gradient option was used. The fluid used for flow field was taken as air, invoking the properties of ideal gas. Operating pressure was set as 1 bar for $M > 0.2$ for the simulation work. The discretisation of momentum equation, energy equation and conservation equation was done using first-order up-winding scheme, pressure-velocity coupling was done using SIMPLE method and k-ε formulation was used for the present analysis. Grid independence study was done at Mach No. 2.5 considering the flow to be inviscid and the optimum grid number was

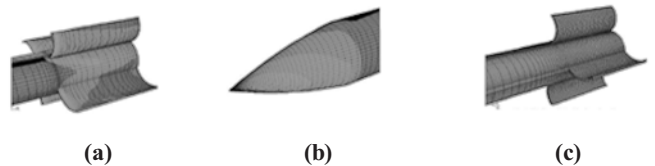


Figure 4. Meshing of curved surfaces: (a) leading edge of the fin (pinched), (b) nose of the projectile, and (c) leading edge of the fin (blunt).

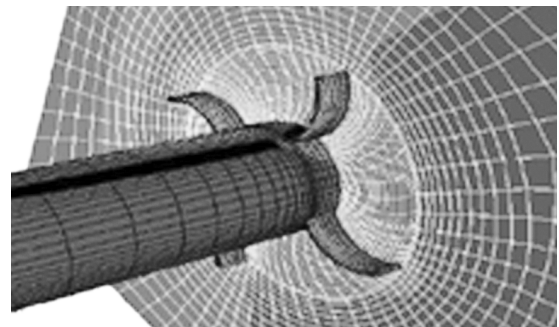


Figure 5. Flow field mesh in the vicinity of fin.

estimated to be 308 000 beyond which the surface pressure does not change with the grid size.

3. RESULTS AND DISCUSSION

To validate the numerical scheme discussed in the previous section, a detailed simulation of the flow over a projectile with WAF was carried out for a Reynolds number range, based on projectile length for sea level conditions, from 27 million to 57 million for free stream Mach number ranging from 1.2 to 2.5. While simulating the flow at varying Mach numbers ranging from transonic to higher supersonic, the flow field solutions showed a number of interesting features. Comparison of computed roll moment coefficients from the present study with the available data in the open literature has been plotted in Fig. 6. As shown in Fig. 6 and Table 1, no consistent roll-reversal point has been reported in the literature. This variation can be attributed to the fact that the previous works were done on different models and at different flow conditions with different

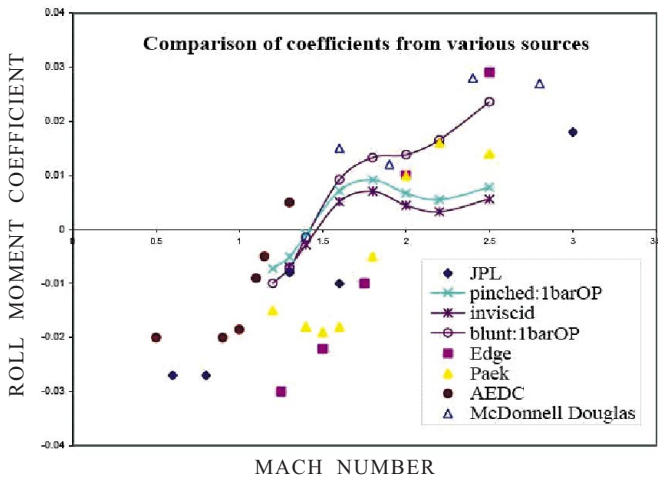


Figure 6. Roll moment coefficient vs. Mach number for the present work and its comparison with other reported works.

assumptions. Paek, *et al.*[13] used the standard TTCP model with blunt leading edge and inviscid conditions using an Euler code, whereas Edge[11] used the standard TTCP configuration with blunt edge but with viscous model using a full Navier-Stokes equation. However, every work shows similar trend, i.e., predicting a cross-over point in low-supersonic range, which is also observed in the present study as shown in Fig. 6.

At lower Mach number, the roll moment coefficients are negative while at higher Mach numbers, roll moment coefficients are positive. A positive roll moment coefficient indicates a roll direction towards fin’s centre of curvature. As shown in Fig. 6, one crossover point is observed, which shows that roll moment coefficients computed with present code agree well with the trend of roll reversal point (crossover point). Furthermore, it agrees well with reports of Abate and Cook[12] that roll moment coefficient curve has small peaks before and after the crossover point.

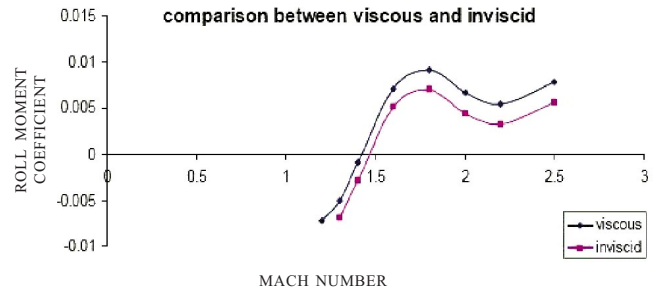
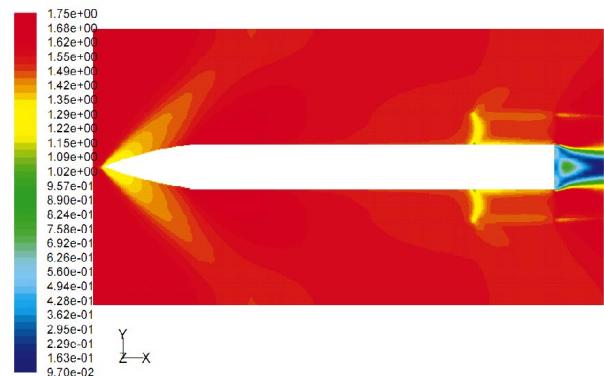


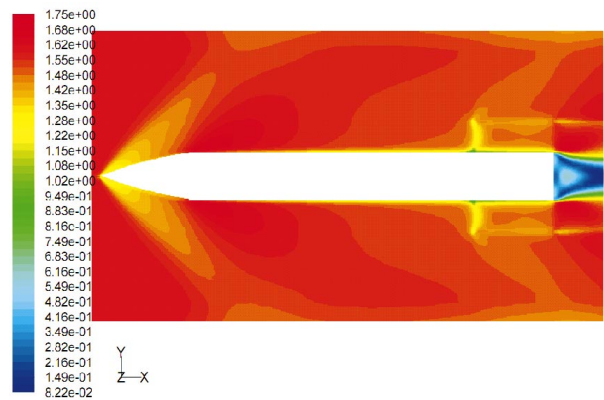
Figure 7. Roll moment coefficient versus Mach number for viscous and inviscid conditions.

The data presented in Figs 6 and 7 for a pinched model shows that the roll reversal Mach number reduces for a viscous flow compared to that of an inviscid simulation. This finding is in contrast to what is seen by comparing the results reported by Paek, *et al* [13], which show exact matching between their inviscid simulation results and the viscous results reported by Edge[11]. The results reported in Figs 6 and 7 are in accordance with what is reported by Tilmann, *et al* [16,17], which shows an increase in the rolling moment coefficient when the viscous effects are considered.

The reduction in the roll reversal Mach number for viscous flows can be attributed to different strengths of



(a)



(b)

Figure 8. Mach number variation over the missile with pinched leading edge fin for a free stream Mach number of 1.6: (a) inviscid solution, (b) viscous solution.

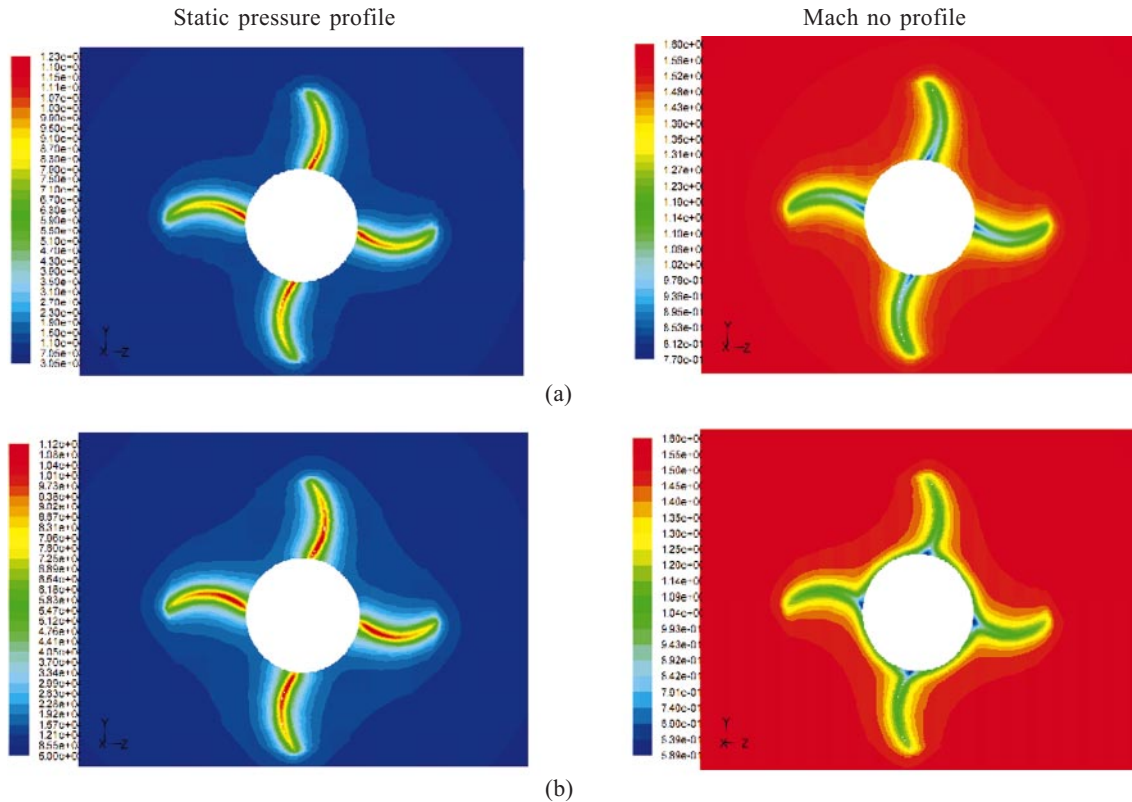


Figure 9. Pressure and Mach number profiles for pinched leading edge model at the leading edge for free stream Mach number of 1.6: (a) inviscid solution, and (b) viscous solution.

the shock waves at the nose of the projectile as well as the frictional losses, bringing in a change in the shock structure in front of the curved fins, as shown in Figs 8(a) and 8(b) and the resulting vortex formation due to pressure built up along the fin curvature as shown in Figs 9(a) and 9(b). This variation of the roll reversal point due to viscous effects may be the cause of the scatter in the data reported so far in the literature as shown in Table 1 and Fig. 6.

Another interesting feature of the data presented in Fig. 6 is that the roll reversal point is the same for both the pinched and blunt fin models. This suggests that the roll reversal is primarily a function of the upstream flow

conditions and is not effected much by the shape of the fin leading edge. However, the magnitude of the rolling moment coefficient for a blunt fin is higher at higher Mach numbers compared to that produced by a pinched fin model.

To understand the reason behind rolling moment generation at zero AOA, a comparative study of the Mach number and pressure profiles were done for both blunt and pinched leading edge models along the body axis. Figures 10(a) and 10(b) show the Mach number profile for the pinched and the blunt leading edge respectively. In the pinched model, one can observe the formation of conical shock at the projectile nose followed by an expansion wave and a

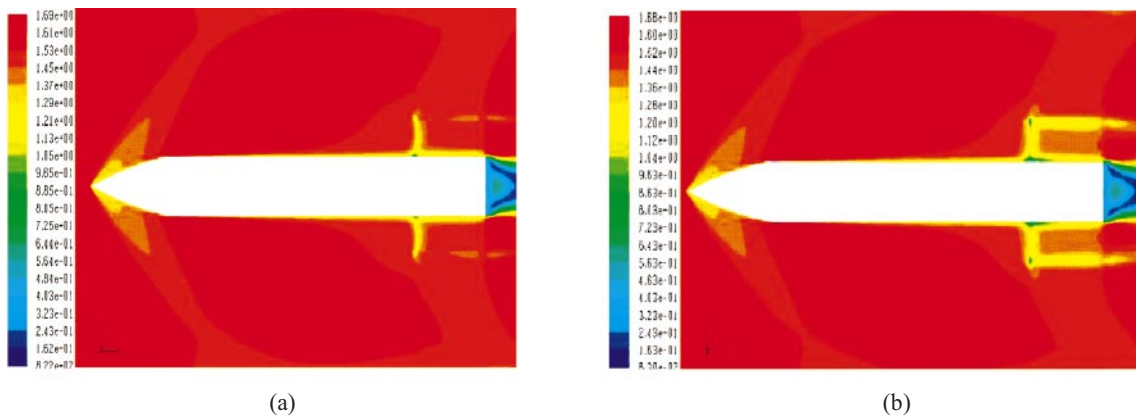


Figure 10. Mach number profile along the projectile for a free stream Mach number of 1.6: (a) pinched leading edge model, and (b) blunt leading edge model.

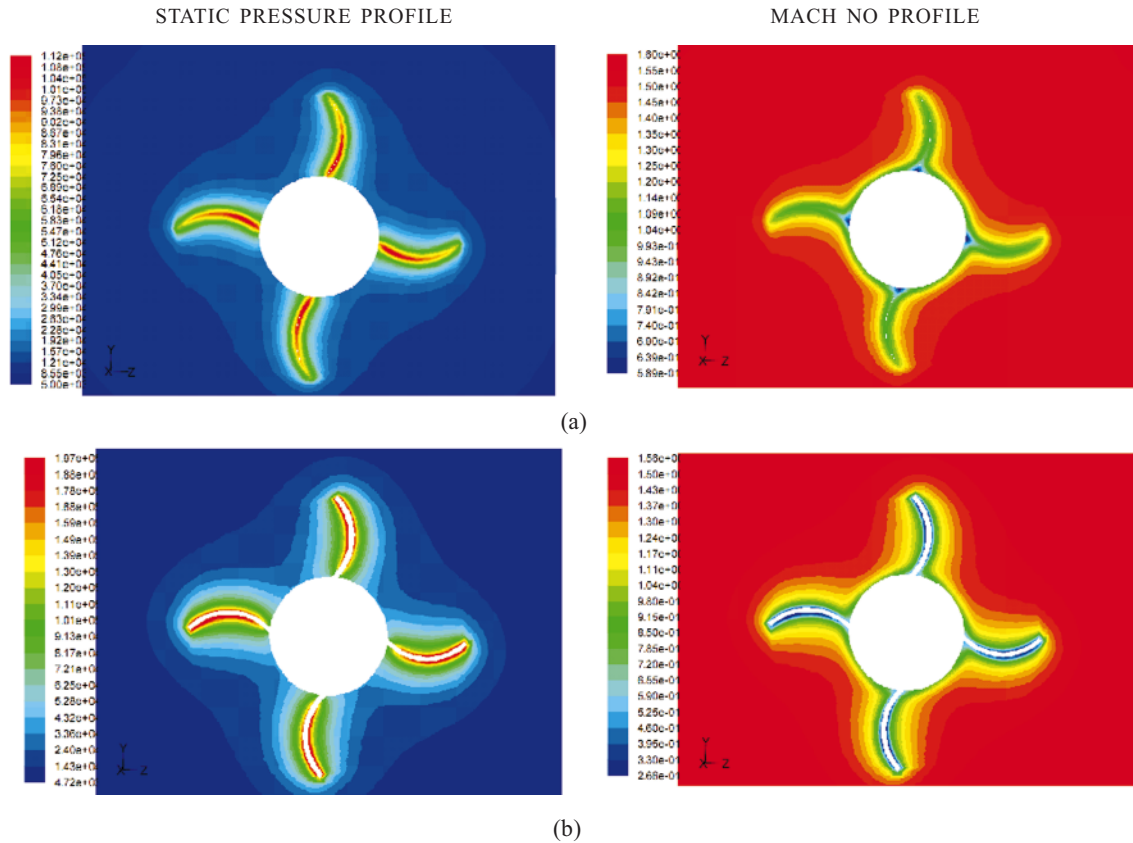


Figure 11. Pressure and Mach number profiles for free stream Mach number of 1.6 at the leading edge: (a) pinched model, and (b) blunt model.

relatively weaker shock in front of the fins. The flow through the curved fins remains primarily supersonic with small zones of subsonic flow at the fin-body junction (as was reported by Tilmann, *et al.*[17]) and towards the tip of the fin. The small region of subsonic flow in the tip region of the fin suggests the formation of a curved shock wave of variable strength from the root to the tip of the fin. The subsonic flow at the fin-body junction is due to the viscous retardation of the flow whereas the subsonic flow towards the fin tip is due to the higher incoming flow Mach number away from the body resulting in the formation of a stronger shock wave.

The presence of the supersonic flow in the fin passage (due to weak oblique shock along the fin leading edge) can be easily corroborated by the presence of the large supersonic patch at the end of the body (expansion plane) as seen in Fig. 10(a). In the case of a blunt fin model, a larger subsonic patch can be observed towards the fin tip. The blunt tip of the fin is expected to produce a detached bow shock, stronger than the oblique shock, when immersed in a supersonic flow. The stronger shock is expected to retard the flow to a subsonic flow, resulting in a smaller zone of supersonic flow through the fin passage. The smaller zone of supersonic flow can be clearly seen in Fig. 10(b) in the much confined expansion to the supersonic flow at the end of the projectile. Once again, the non-uniform Mach number profile at the fin plane suggests

the presence of a curved shock of varying strength from the fin root to tip. The difference in the rolling moment for the pinched and blunt tip models suggest that the non-zero rolling moment is not only due to the vortex formation reported by Tilmann, *et al.*[17] but the fin leading edge shape also plays an important role by dictating the leading edge shock structure, as reported by Winchenbach, *et al.*[15], responsible for flow retardation away from the fin-body junction. The difference in fluid dynamics for a pinched leading edge model and a blunt leading edge model is further illustrated in Figs. 11 (a-b) in which the static pressure and Mach number profiles at the leading edge are plotted.

Since the pinched fin model provides a lower rolling moment compared to the blunt fin model, and therefore, is expected to be aerodynamically more stable, the phenomenon of roll reversal with Mach number was studied for a pinched fin model. The results presented hereafter are all for the pinched fin model. It can be seen in the data presented in Fig. 6 that the roll reversal for this model at zero degree AOA attack occurs between Mach 1.4 and 1.5. Furthermore, as shown in Fig. 6 and discussed in the subsequent discussion, the point of roll reversal is found to be independent of the fin tip shape, i.e., same roll reversal point is observed for both the pinched and the blunt fin models. This observation suggests that the roll reversal is dependent on the flow dynamics upstream of the fins. To understand this flow field, Mach number as well as static pressure variations

for different free stream Mach numbers have been plotted along a line parallel to the missile body up to the middle of the fin tip. From the Mach number variation (as shown in Fig.12 (a)) it can be observed that the flow is subsonic for inlet condition of up to Mach No. 1.4 just before the fin whereas the flow remains supersonic even up to the fin for Mach No. 1.5 and above. Hence, there is a transition from subsonic to supersonic flow just before the fin-tip in the Mach number from 1.4 to 1.5. This transition from subsonic to supersonic flow just before the fin seems to be the primary cause for the roll reversal.

The static pressure profile (as shown in Fig. 12(b)) indicates the formation of shock waves just before the fin with the sharp increase in pressure. Since the flow remains supersonic for Mach numbers beyond 1.5, this shock should be oblique shock or detached bow shock. This observation confirms the converging-diverging nozzle analogy suggested by Abate and Cook[12] showing that the roll reversal indeed happens at a fin tip Mach number of 1.0. However, the fin tip Mach number is different from the free stream Mach number and depends on the body geometry and flow conditions.

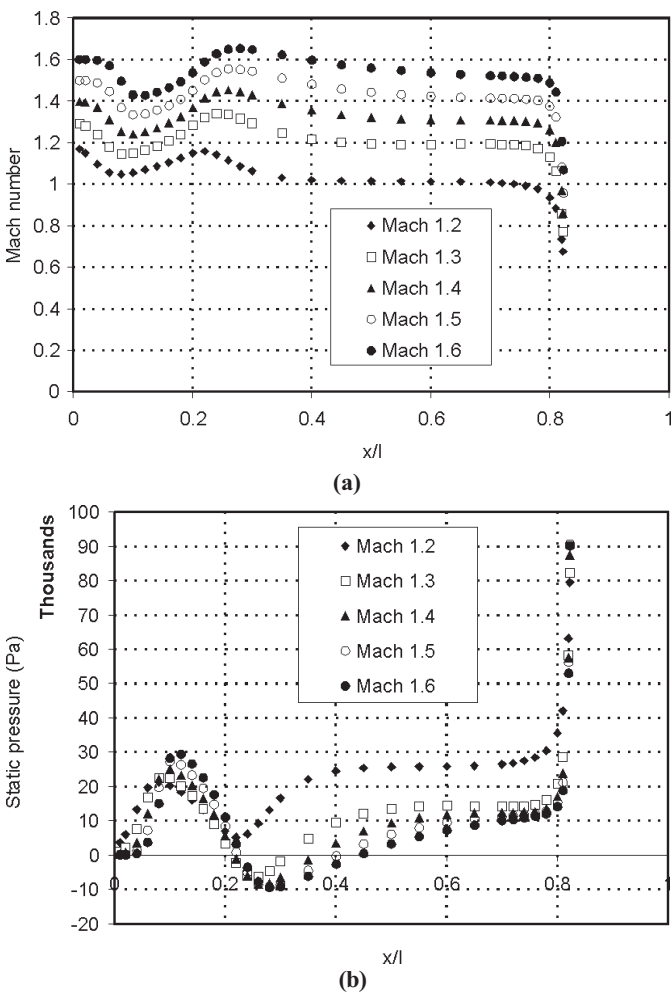


Figure 12. Mach number and static pressure profile along the body (at the mid plain of the fin) for different free stream Mach numbers: (a) Mach number and (b) static pressure.

To further understand the flow field, the Mach number variations are plotted along fin curvature for different axial locations before and after the fin, as shown in the Figs 13 (a) and 13(b). Here chordwise direction is non-dimensionalized with the chord length of the fin and spanwise direction along the fin curvature is non-dimensionalized with the curved length of the fin. It has been observed (as shown in Fig.13(a)) that for $x/c = -0.05$ (just before the fin tip) the flow for Mach number 1.3 and above is supersonic in most parts of the fin and subsonic close to the body surface. However, at $x/c = 0$ (at the fin tip), the flow is completely subsonic up to Mach No. 1.4 while it is partially supersonic for Mach No. 1.5 and above (as shown in Fig.13 (b)). This further validates the observed roll reversal phenomenon in the range of Mach No. 1.4 to 1.5 and illustrates the difference between the flow fields before and after the roll reversal points. Also, along the fin curvature a varying flow field has been observed. This is due to the varying shock strength as one moves away from the surface along the fin curvature.

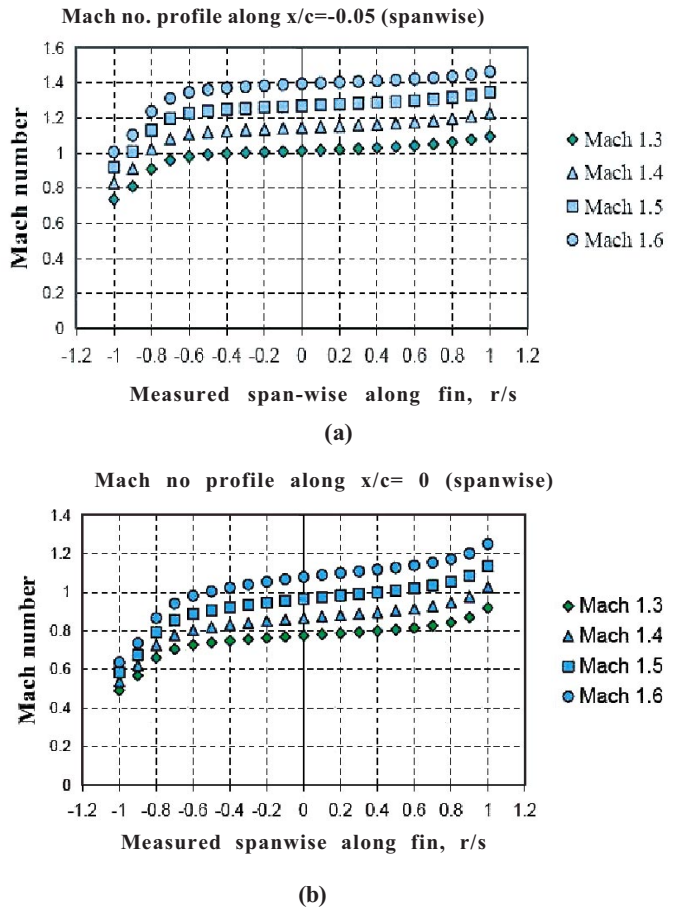


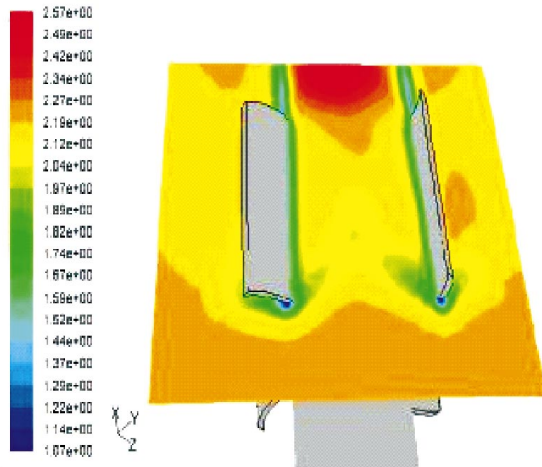
Figure 13. Mach number variation in span-wise direction (mid-span = 0.0) for different free stream Mach numbers: (a) $x/c = -0.05$ and (b) $x/c = 0.0$.

Detailed analysis of the flow field has been done by plotting the contours of Mach number and static pressure at different sections, which has been discussed. Figures 14(a) and 14(b) show Mach number profiles of the fin

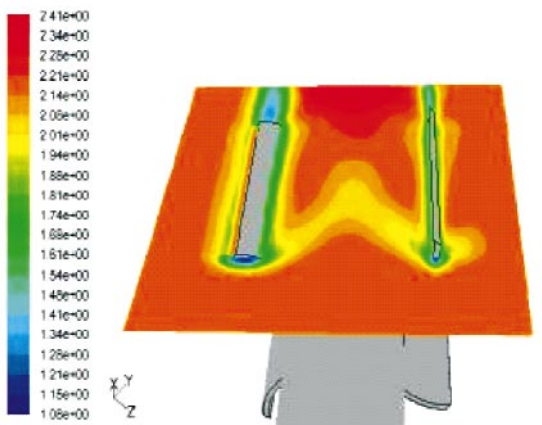
passage for a free stream Mach number of 2.2. Where, Fig.14 (a) shows Mach number contours at mid-span of the fin, Fig.14 (b) shows the same at 90 per cent span of fin. These contours show a good indication of shock structure generated by the modelled WAF. As one moves along the fin curvature along radial direction, shock strength varies. Moving radially outward, the strength of shock wave decreases along concave region of the fin, whereas it remains the same in the convex region of the fin. On the convex side of the fin, the shock wave expands whereas it converges on the concave side of the fin. Moving outwards radially, this continuously changing converging flow leads to local deposition of flow inside bowl of the fin, causing pressure rise in the vicinity of the concave side of the fin, as compared to the convex side of the fin, where normal expansion of flow causes pressure release, as observed in the Figs 15(a) and 15(b), which show static pressure profile in the fin passage for a free stream Mach number of 2.2 at the mid-span and 90 per cent span, respectively. This imbalance of pressure, when integrated along the whole span of the fin, results in

generation of rolling moment even for axisymmetric flow. Another interesting feature of the results presented in Figures 14 and 15 is that the flow initially slows down in the fin passage and then accelerates again in the direction of the flow, as seen in the initial decrease in the flow Mach number followed by an increase along the flow direction (Fig. 14) and corresponding increase and subsequent decrease in the pressure, as shown in Fig. 15.

To further elaborate this observation, the flow field was resolved at different chord locations along the axis in the fin passage and the results have been presented in Figures 16, 17, and 18 for different free stream Mach numbers, which show static pressure and Mach number profiles at various chord lengths of 15 per cent, 20 per cent, 25 per cent, 35 per cent, 50 per cent, and 75 per cent at free stream Mach numbers of 1.2, 1.4, and 2.2 respectively. At 15 per cent chord for Mach No. 1.2, pressure is low in the concave side of the fin as compared to convex side of fin, resulting in generation of negative rolling moment, as seen in Fig. 6. Further downstream of the chord till

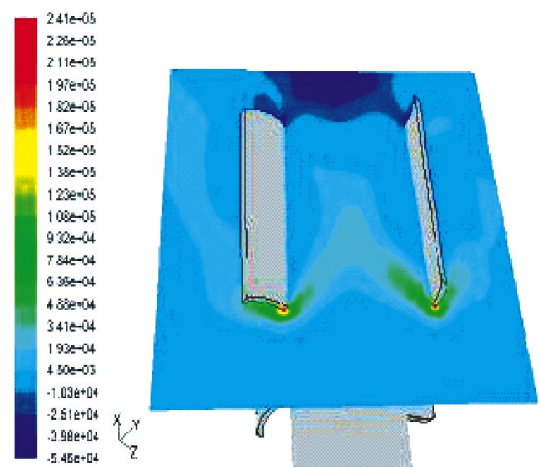


(a)

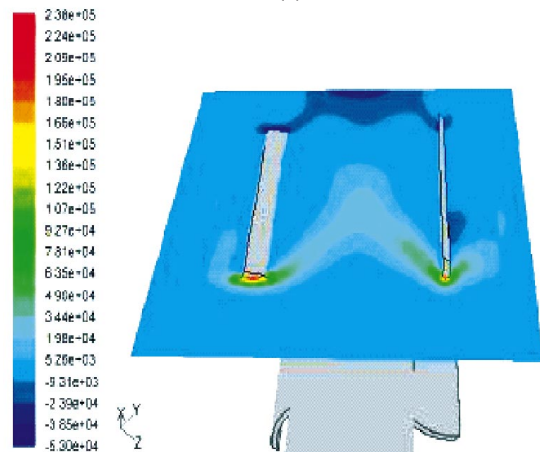


(b)

Figure 14. Mach number variation in the fin passage for a free stream Mach number of 2.2: (a) at mid-span and (b) at 90 per cent span.



(a)



(b)

Figure 15. Static pressure profile in the fin passage for a free stream Mach number of 2.2: (a) at the mid-span and (b) at 90 per cent span.

25 per cent chord, this difference is quite substantial. However, further downstream the flow from the convex surface of the neighboring fin interacts with the concave surface flow, which nullifies the effect of rolling moment generation with the diffusion of both flows. This is what is observed in the Figures 16(d) to 16(f). Thus the rolling moment generation is largely due to uneven pressure distribution along both sides of fins in-between 5 per cent to 35 per cent of the chord. Similarly at Mach No. 1.4 (near about cross-over point) same trends have been observed, as shown in Figures 17(a) to 17(f). Till the quarter-chord of the fin (see Fig.17b) there is not much moment generation, whereas much of rolling moment generation can be attributed to

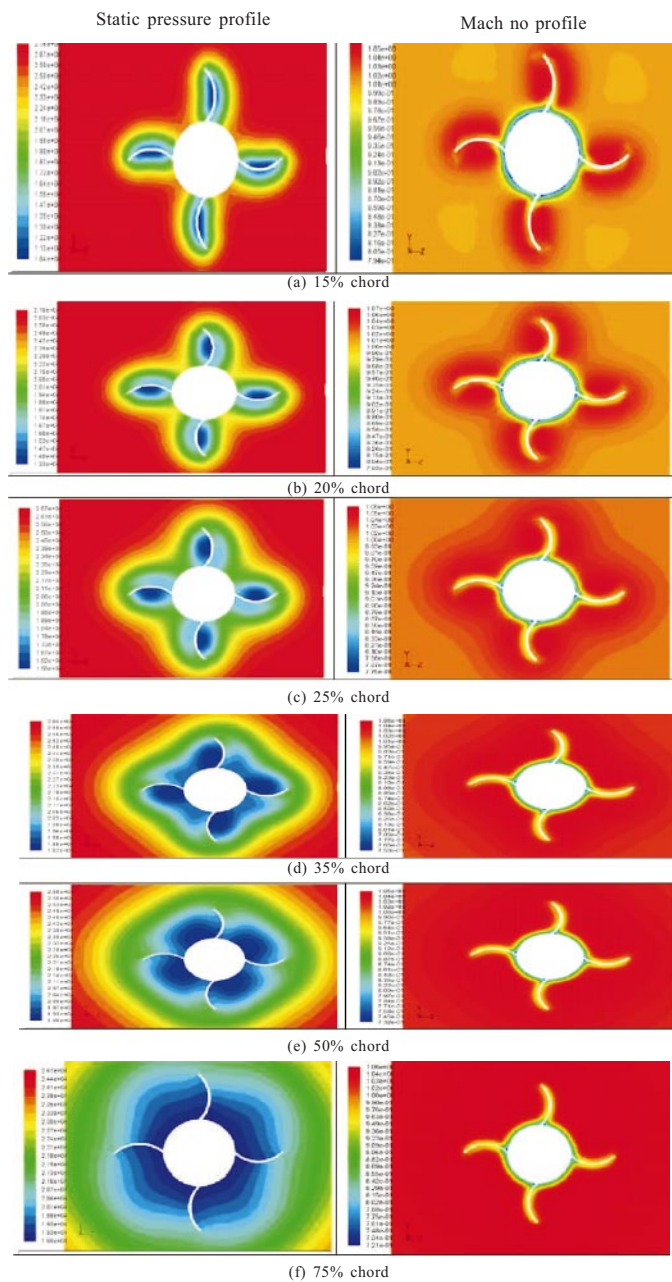


Figure 16. Pressure and Mach number profile at different axial (chord) location for Mach 1.2.

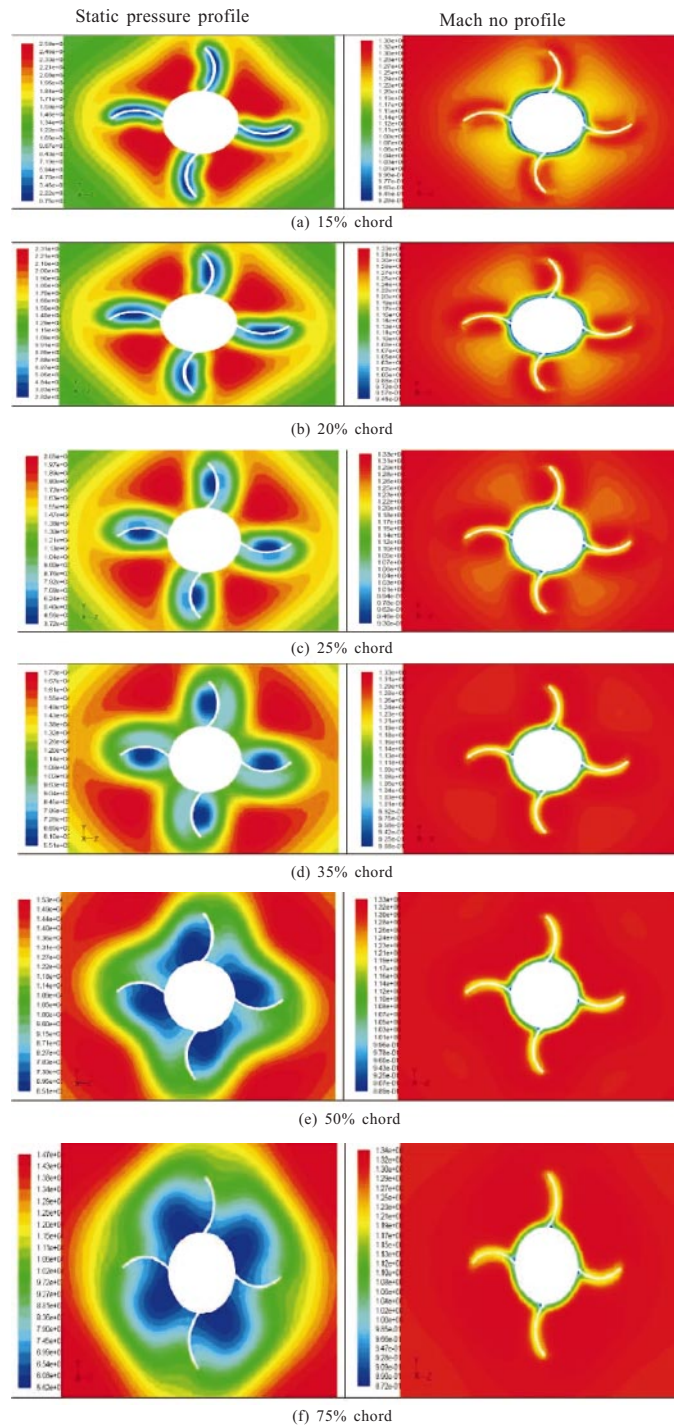


Figure 17. Pressure and Mach number profile at different axial (chord) locations for Mach number 1.4 (cross-over point).

the pressure difference produced in between 25 per cent to 35 per cent of chord (Figs 17(c) and 17(d)). Again, the convex side flow converges with the concave side flow of the other fin, resulting in reduction of rolling moment in these sections. As shown in Figures 18(a) to 18(f) for the Mach number 2.2, there is a high-pressure region in the concave side of fin than the convex side from the leading edge itself [Fig. 18(a)]. It grows to a larger value somewhere in between 20 per cent of the chord [Fig.18(b)]. However

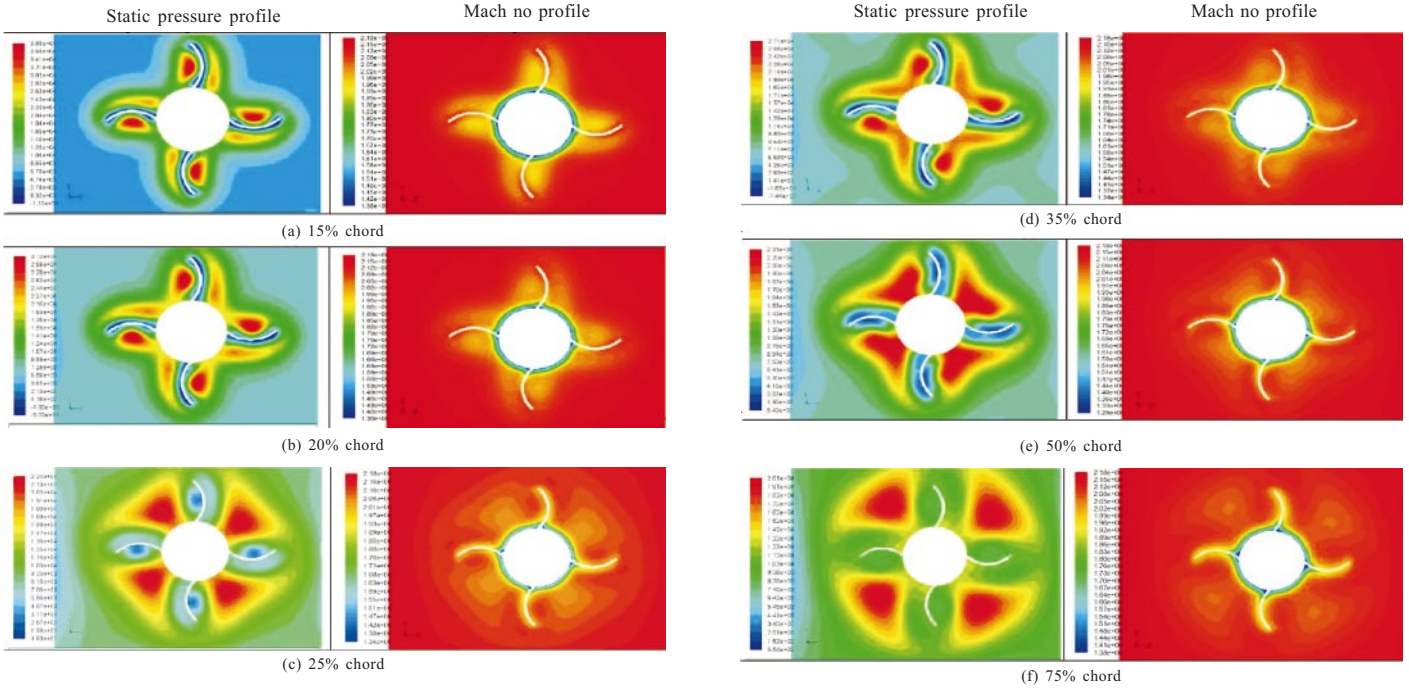


Figure 18. Pressure and Mach number profiles at different axial (chord) locations for Mach 2.2.

in this case, the diffusion starts as early at about 25 per cent chord [Fig. 18(c)], which causes reduction in rolling moment values [Figs. 18(d) to 18(f)].

Figures 19 and 20 show the Mach number and static pressure profiles at the root of the fin, at the mid-span, and at the tip-end of the fin for free stream Mach numbers

of 1.2 and 1.4 in order to understand the roll reversal phenomenon. The results presented in Fig. 19(a) for Mach number 1.2 show that the flow Mach number in the fin passage monotonically increases in the flow passage (except in the boundary layer and behind the detached bow shock) with a corresponding monotonic drop in the pressure, as

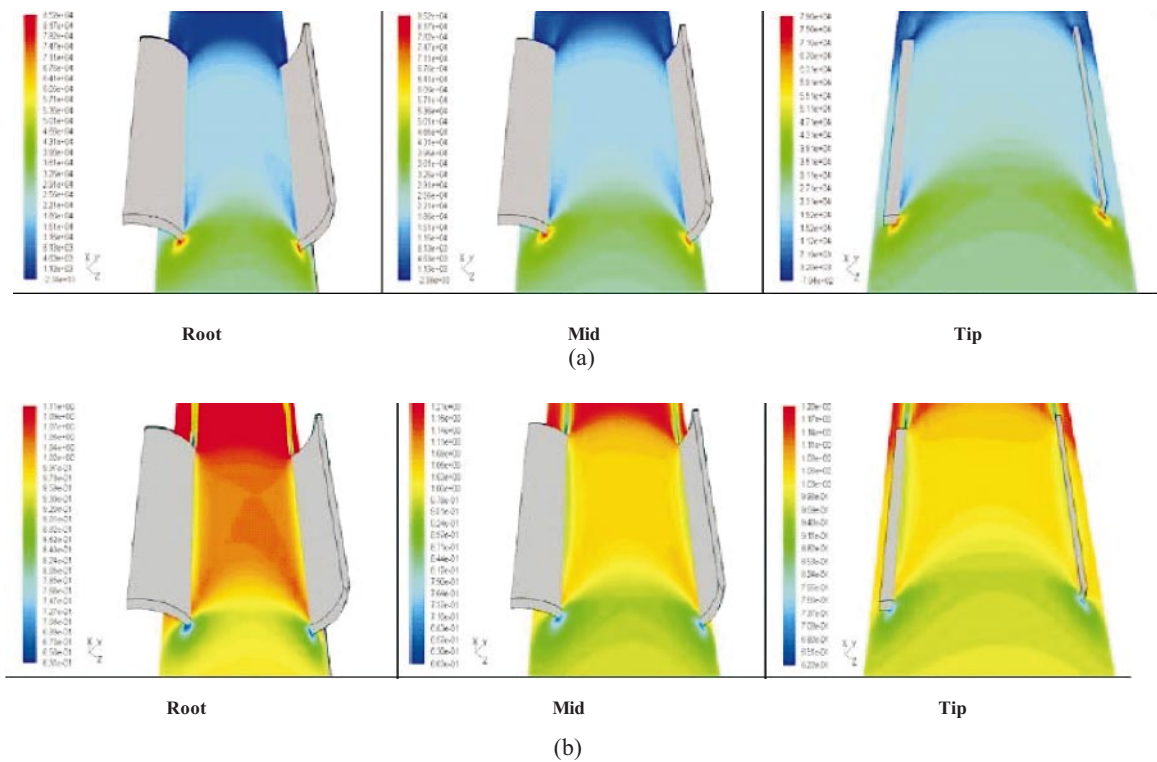


Figure 19. Mach number and static pressure variations in the fin passage at different spanwise location for free stream Mach number of 1.2: (a) Mach number, and (b) static pressure.

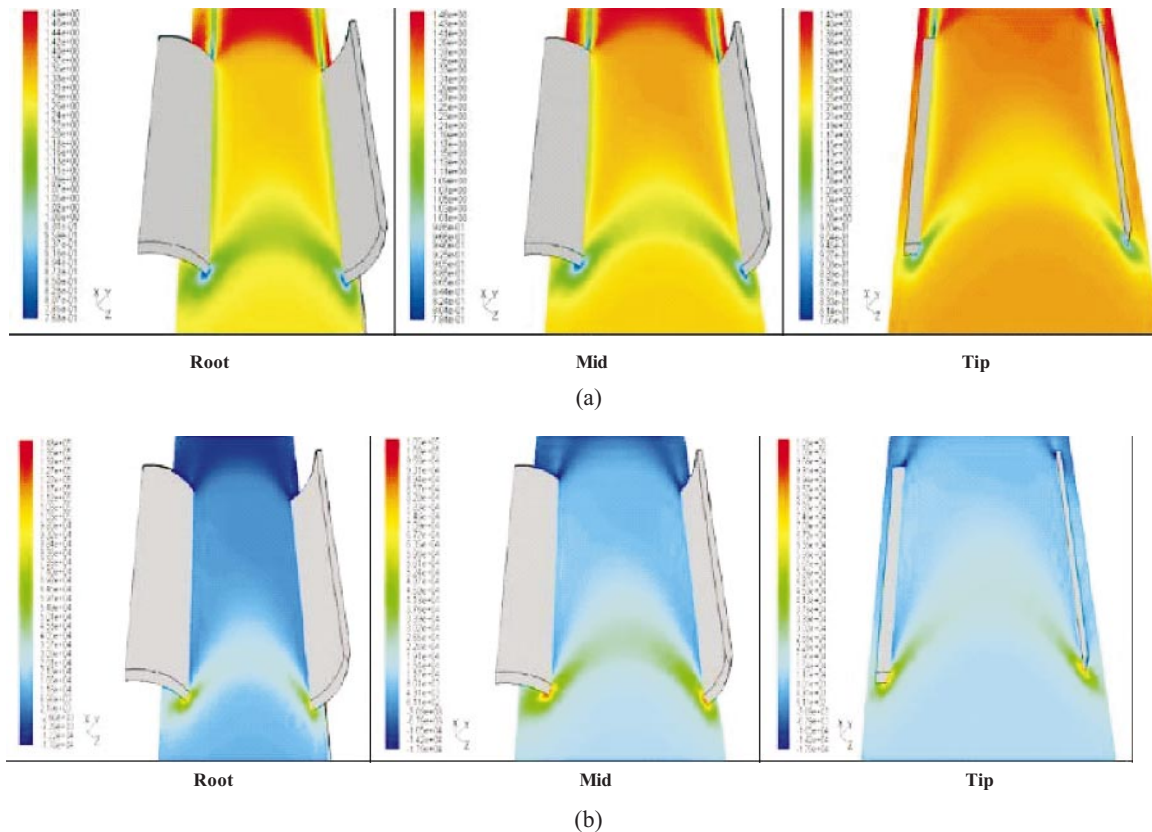


Figure 20. Mach number and static pressure variations in the fin passage at different spanwise locations for free stream Mach number of 1.4: (a) Mach number and (b) static pressure.

shown in Fig. 19(b). However, once we go beyond the roll reversal point (i.e., Mach 1.4), the passage Mach number first decreases up to a certain length and then starts to increase again with corresponding increase and decrease in static pressure, as seen in Figures 20(a) and 20(b). This phenomenon conclusively points to the fact that indeed there is a change in the nature of the flow in the fin passage, particularly towards the leading edge of the fins up to a fraction of the chord that give rise to the roll reversal.

To further elaborate the findings, the static pressure profile has been plotted along a line midway at the span of the fin, both on the concave and the convex sides for free stream Mach numbers 1.2 to 1.8, as shown in Fig. 21. As shown in Fig. 21 (a), the convex side has greater pressure than the concave side in most of the part except at the small fin tip region where concave side pressure slightly exceeds the one on the convex side. Figures 21(b) and 21(d) show that as the Mach number increase, this difference between the static pressure at the concave and convex sides at the fin leading edge region goes on building up whereas it remains mostly the same in the other part. Therefore, it can be safely concluded that this change in the static pressure, at the fin leading edge region, plays a major role in causing the roll-reversal phenomenon.

This study shows that the anomalies present in the flow over projectiles with WAFs is a complex viscous-compressible flow and is governed by the flow Mach

number and the body geometry. The complex nature of the flow field and the presence of curved bow shock is perhaps the reason that there is so much scatter in the data reported so far by various researchers as it is almost impossible to maintain the same conditions for two studies. Therefore, it can be concluded that the roll reversal and non-zero rolling moment at zero angle of attack are system level problems in the projectiles with wrap around fins, and hence, detailed analysis must be done to estimate the aerodynamic coefficients of a particular configuration.

4. CONCLUSIONS

Flow field solutions of a projectile with WAFs were obtained by solving 3-D Navier-Stokes equations. Grids were accurately distributed across the flow field, both near the tip of the nose and at the fin edge of a TTCF model. The roll moment coefficients were calculated from flow field solutions and then compared with experimental results. Computed roll coefficients show a similar trend of roll reversal in low-supersonic range, as obtained in experimental results reported in the literature. A detailed study of the flow field at different Mach numbers were carried out and it was observed that roll reversal phenomenon is largely due to the shock wave structure in the vicinity of fin-body junction making the flow in between the fin passage change its nature for subsonic and supersonic flows just upstream of the fins. Furthermore, the difference in the dynamics of the flow in the concave and convex sides of the fins

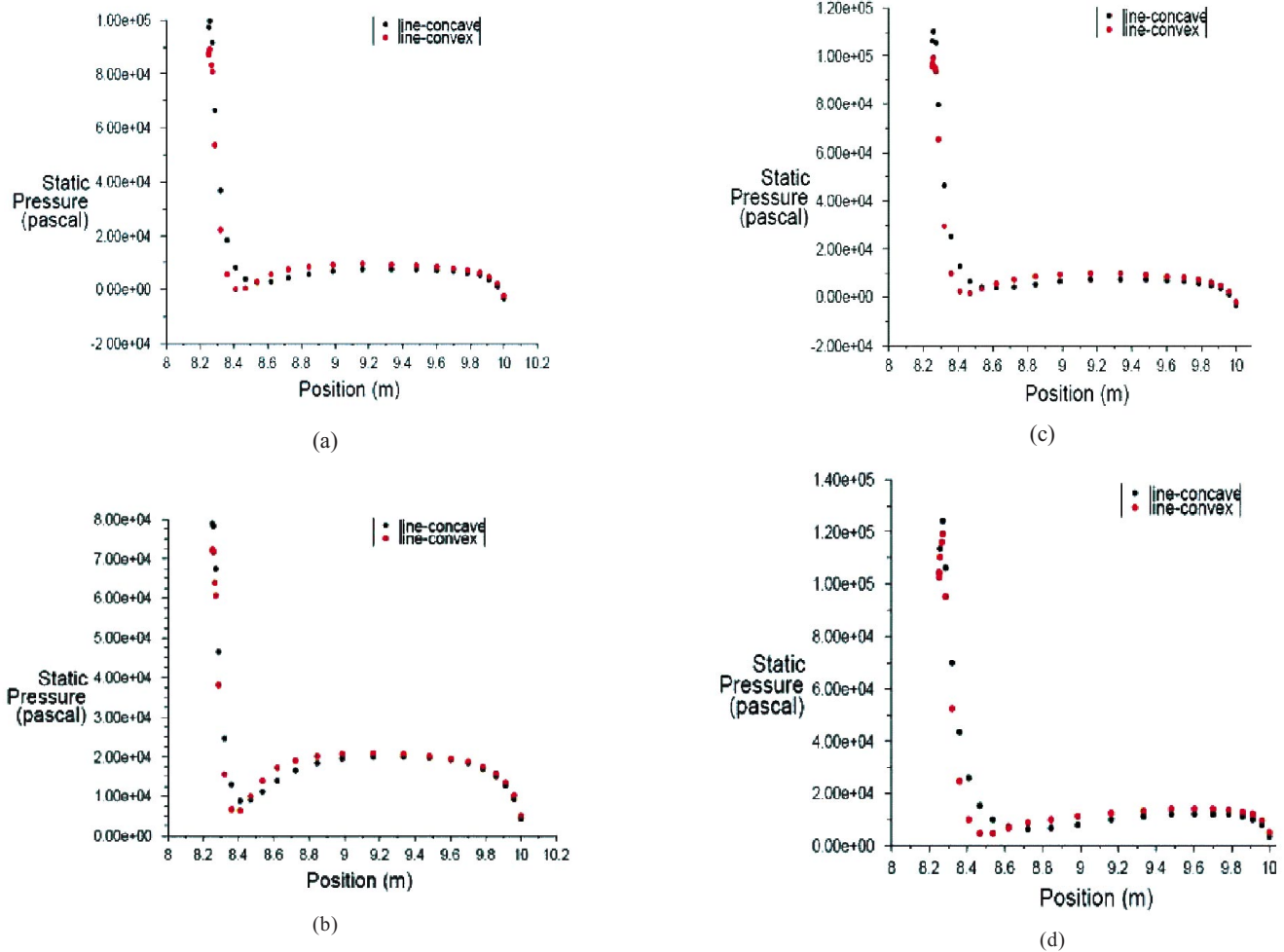


Figure 21. Static pressure variation over a fin surface for concave and convex sides at the mid-span for different free stream Mach numbers: (a) $M = 1.2$, (b) $M = 1.4$, (c) $M = 1.5$, and (d) $M = 1.8$.

cause pressure buildups responsible for non-zero rolling moments at zero angle of attack. The study also illustrates that only the frontal portion of the fins, and not the whole fins, take part in the processes responsible for rolling moment generation. With varying edge and tip shape (blunt edge and 45° edge on the fin), roll-reversal point remains the same, but magnitude varies significantly at higher Mach numbers.

ACKNOWLEDGEMENT

This project was funded by the EMCB Panel of Armament Research Board of DRDO.

REFERENCES

1. McIntyre, T.C.; Bowersox, R.D.W. & Goss, L.P. Effects of Mach number on supersonic wrap-around fin aerodynamics. *J. Spacecraft Rockets*, 1998, **35**(6), 742-48.
2. Catani, U.; Bertin, J.J.; Whyte, R.H. & Hathaway, W.H. Aerodynamics characteristics for a slender missile with wrap-around fins. *Journal of Spacecraft*, 1986, **9**(6), 627-32.
3. Tanrikulu, O. & Mahmutyazicioglu, G. Wrap-around finned missiles - neat but nasty. In AIAA Atmospheric Flight Mechanics Conference, 11-13 August 1997, New Orleans, LA. AIAA-1997-3493.
4. Lucero, E.F. Subsonic stability and control characteristics of configuration incorporating wrap around surfaces. *Journal of Spacecraft*, 1976, **13**(12), 740-45.
5. Bar-Haim, B. & Seginer, A. Aerodynamics of wraparound fins. *Journal of Spacecraft*, 1983, **20**(4), 339-45.
6. Kim, Y.H. & Winchenbach, G.L. Roll motion of a wraparound fin configuration at subsonic and transonic mach numbers. *Journal of Guidance*, 1985, **9**(2), 253-55.
7. Tanrikulu, O.; Onen, C. & Gokhan, T. Nonlinear yaw-pitch-roll coupling of unguided missile with wraparound fins. *J. Spacecraft Rockets*, 2000, **37**(6), 731-39.
8. Tanrikulu, O. & Mahmutyazicioglu, G. Magnus effects on stability of wraparound-finned missiles. *J. Spacecraft Rockets*, 1998, **35**(4), 467-72.
9. Vitale, R.E.; Abate, G.L.; Winchenbach, G.L. & Riner, W. Aerodynamics test and analysis of a missile configuration with curved fins. AIAA Paper No. 92-4495, 1992.

10. Wardlaw, A.B.; Priolo, F.J. & Solomon, J.M. Multiple-Zone strategy for supersonic missiles. *J. Spacecraft Rockets*, 1987, **24**(4), 377-84.
11. Edge, H.L. Computation of the roll moment for a projectile with wrap-around fins. *J. Spacecraft Rockets*, 1994, **31**(4), 615-20.
12. Abate, G.L. & Cook, T. Analysis of missile configuration with wrap-around fins using computational fluid dynamics. AIAA Paper No. 93-3631-CP, 157-66.
13. Paek, S.K.; Park, T.S.; Bae, J.S.; Lee, I. & Kwon, J.H. Computation of roll moment for projectile with wrap-around fins using euler equations. *J. Spacecraft and Rockets*, 1999, **36**(1), 53-8.
14. Dahlke, C.W. The Aerodynamics characteristics of wrap-around fins at Mach numbers of 0.3-3.0. US Army Missile Command, Redstone Arsenal, AL, Oct. 1976. RD-77-4.
15. Winchenbach, G.L.; Buff, R.S.; Whyte, R.S. & Hathaway, W.H. Subsonic and transonic aerodynamics of a wraparound fin configuration. *Journal of Guidance*, 1986, **9**(6), 627-32.
16. Tilmann, C.P.; Buter, T.A. & Bowersox, R.D.W. Characterization of the flow field near a warp-around fin at Mach 2.8. *Journal of Aircraft*, 1998, **35**(6).
17. Tilmann, C.P.; Huffman Jr., R.E.; Buter, T.A. & Bowersox, R.D.W. Experimental investigation of the flow structure near a single wrap around fin. *J. Spacecraft Rockets*, 1997, **34**(6), 729-36.
18. Weiss, J.M. & Smith, W.A. Preconditioning applied to variable and constant density flows. *AIAA Journal*, 1995, **33**(11), 2050-057.
19. Roe, P.L. Characteristic based schemes for the Euler equations. *Annual Rev. Fluid Mech.*, 1986, **18**, 337-65.
20. Weiss, J.M.; Maruszewski, J.P. & Smith, W.A. Implicit solution of the navier-stokes equations on unstructured meshes. In 13th AIAA CFD Conference, July 1997, Snowmass, CO. AIAA Paper No. AIAA-97-2103.
21. Fluent User Manual, 2005.

Contributors



Mr Ravi Krishna received BTech (Aerospace Engg) from Indian Institute of Technology (IIT) Kanpur in 2007. He is Scientist 'B' at Aerial Delivery Research and Development Establishment (ADRDE), Agra. His areas of interest include flight mechanics, aerodynamics, recovery system designing, CFD simulation of high speed flow, and combustion of premixed mixers.



Mr Rhishabh Surit received BTech (Aerospace Engg) from IIT Kanpur in 2007. He is Scientist 'B' at Integrated Test Range (ITR), Chandipur. His areas of interest include flight mechanics, high-speed aerodynamics, real-time trajectory simulation, flight testing, and CFD simulation of high speed flow.



Dr Abhijit Kushari received PhD (Mechanical Engg) from Georgia Tech in 2000. He is an Associate Professor in the Department of Aerospace Engineering at IIT Kanpur. His research interests are aerospace propulsion, combustion, and high speed flows.



Dr A.K. Ghosh received BTech, MTech and PhD from IIT Kanpur. He is a Professor in the Department of Aerospace Engineering at IIT Kanpur. His areas of interest are flight mechanics, flight testing, parameter estimation from real flight data, and neural networks.